ScienceAdvances

AAAS

Supplementary Materials for

Dramatic influence of curvature of nanowire on chiral domain wall velocity

Chirag Garg, See-Hun Yang, Timothy Phung, Aakash Pushp, Stuart S. P. Parkin

The PDF file includes:

Other Supplementary Material for this manuscript includes the following:
(available at advances.sciencemag.org/cgi/content/full/3/5/e1602804/DC1)

Supplementary Text

1.   Quasi two-dimensional model for current driven domain wall dynamics in circular curved wires

The one-dimensional model (*26*, *33*) is a useful theoretical tool to understand current driven domain wall (DW) dynamics both intuitively and quantitatively. This model has been successfully used to describe the current induced motion of DWs in straight racetracks formed from single magnetic layers with perpendicular magnetic anisotropy (PMA) via a chiral spin torque (*14*, *20*), and in synthetic ferromagnets and antiferromagnets via an exchange coupling torque (*21*). Here we extend this model to the quasi two-dimensional model (Q2D) to curved nanowires by incorporating (1) a moving reference frame with Cartesian coordinates that allows for tilting of the DW to be taken into account, (2) periodic variation in anisotropy to simulate DW pinning, (3) thermal fluctuations in the DW position and magnetization along the wire, and (4) a non-uniform current density transverse to the wire.

The basic assumption of our model is that if the DW width is much smaller than the radius of curvature, the DW has a fixed magnetization profile of polar angle θ by which the magnetization is rotated from the direction perpendicular to the layer, i.e. the z-axis, and the azimuthal magnetization angle ψ is uniform all over the wire at each instant of time when it is manipulated either by current or magnetic field or a combination of the two. In contrast, when the DW width becomes comparable to the radius of curvature of the wire, an additional curvature effect should be taken into account since the azimuthal magnetization angle within DW does not look uniform anymore in the curved wire moving frame coordinate. However, the wires used in our experiment have a few microns of curved radius whilst the DW width parameter is ~ 5 nm. Hence the former assumption is valid since the latter effect is vanishingly small and neglected hereafter. For the case of perpendicularly magnetized nanowires the DW dynamics can be described within the Q2D model by three parameters, namely the position q of the DW along the nanowire, its conjugate momentum $2M_s\psi/\gamma$, where ψ is the angle of the DW's magnetization in the plane of the wire with respect to the direction $\hat{x}$, and the tilting angle χ defined with respect to the direction $-\hat{y}$ (see fig. S1). M_s is the saturation magnetization and γ is the gyromagnetic

ratio. Here, the key point to note is that the DW motion in curved wires are instantaneously governed by the DW magnetization angle ϕ, and tilting angle ζ, defined with respect to unit vectors, $\hat{e}_s$, $\hat{e}_r$ and $\hat{z}$ in the moving frame coordinates but the DW dynamics is ultimately described by the static Cartesian coordinates in Q2D model because $\hat{e}_s$ and $\hat{e}_r$ vary as a function of time and DW position. ϕ and ζ are connected to the corresponding parameters, ψ and χ, defined in static Cartesian coordinates, respectively, via DW position q : $\phi(t) = \frac{q(t)}{R} + \psi(t)$ and $\zeta(t) = \frac{q(t)}{R} + \chi(t)$ where R is the mid-radius of wire (see fig. S1). As a result, the domain wall profile of curved wires in terms of moving frame parameters is given by

$$\theta(r,t) = 2 \arctan \exp \left[\pm \frac{r\left(\xi - \frac{q(t)}{R}\right) \cos \zeta(t) + (r-R)\sin \zeta(t)}{\Delta} \right] \tag{1}$$

This can be rewritten in static Cartesian coordinates as following

$$\theta(x,y,t) = 2 \arctan \exp \left[\pm \frac{\left(\sqrt{x^2+y^2}\arctan\frac{y}{x}-q(t)\right)\cos\left(\frac{q(t)}{\sqrt{x^2+y^2}}+\chi(t)\right) + \left(\sqrt{x^2+y^2}-R\right)\sin\left(\frac{q(t)}{\sqrt{x^2+y^2}}+\chi(t)\right)}{\Delta} \right]$$

$$\tag{2}$$

Here the upper and lower signs correspond to the $\odot \,|\, \otimes$ and $\otimes \,|\, \odot$ domain magnetic configurations, respectively, and Δ is the domain wall width parameter. It should be noted that the azimuthal magnetization angles $\phi(t)$ and $\psi(t)$ do not depend on spatial parameters, r, x, and y, i.e. uniform as mentioned above. Consequently, the DW defined by Eq. (1) is not a straight line as seen in fig. S1 since the DW tilt angle ζ in moving coordinates is constant along the transverse to the wire direction thus showing that the tangent of DW at each point along the DW keeps the same angle with $-\hat{e}_r$ direction.

Before deriving the equations of motion, let us first discuss the additional effects as shown in section **a-c** that we have taken into account in development of Q2D model in curved wires.

a. Non-uniform anisotropy induced pinning effect

The threshold current density above which the DWs start to be depinned and move by current is zero in the absence of any pinning (e.g. see fig. S5). Since the curved nanowire devices we measured do not have any artificial notches or blips, we consider the intrinsic DW pinning only. There are various intrinsic sources that cause DW pinning. Among them we make use of the periodic variation of anisotropy $K_{eff} = K_{eff}^0 \left[1 - \eta \cos \frac{2\pi(q-q_s)}{q_0}\right]$ along the length of wire to simulate pinning since it is the major factor that give rise to the broadening of ferromagnetic resonances (FMR) spectrum linewidth, that is, so-called inhomogeneous broadening. Here η, q_s and q_0 are the strength, center position and period of anisotropy, respectively (see fig.S2). The pinning field induced by the periodic anisotropy is $H_{pin} = \frac{4\pi\Delta\eta K_{eff}^0}{q_0 M_s}$ where M_s is the saturation magnetization. Based on our fitted parameters, we have $H_{pin} \sim 560$ Oe that is consistent with 5-10% of anisotropy field $H_K \sim 1$ T of our film since the inhomogeneous broadening is known to correspond to this proportion of H_K (*34*).

b. Thermal broadening

At finite temperatures, thermal fluctuations are known to induce normal distributions (Gaussians) of the initial position q and magnetization angle ψ of DW (*35*). The distribution Gaussians can be derived as (see fig. S3A,B)

$$P(q_{initial}) = \sqrt{\frac{M_s H_{c0} w t_m}{\pi q_0 k_B T}} \exp\left(\frac{M_s H_{c0} w t_m q_{initial}^2}{q_0 k_B T}\right)$$

$$Z(q_{initial}) = \sqrt{\frac{M_s H_{c0} w t_m \Delta}{2 k_B T}} \exp\left(\frac{M_s H_{c0} w t_m \Delta \psi_{initial}^2}{q_0 k_B T}\right)$$

where w is the width of wire, t_m is the thickness of magnetic film, H_{c0} is the propagation field, k_B is the Boltzmann constant, $q_{initial}$ and $\psi_{initial}$ are the initial condition of DW position and azimuthal angle of magnetization, respectively. Since the sample temperature T is proportional to

the power applied to the wire, $T \propto J^2$, where J is the current density and we use $T(J = 0)$=300 K, and $T(J = 2 \times 10^8 \ A/cm^2)$=500 K (see fig. S3C).

The thermal broadening effect is implemented in the Q2D model by meshing $q_{initial}$ and $\psi_{initial}$ around $q_{initial} = 0$ and $\psi_{initial} = 0$, calculating the results at each mesh point and then averaging them weighted by the Gaussians as following

$$\langle X \rangle = \frac{\sum_{i,j} X_{ij} P(q_{initial,i}) Z(\psi_{initial,j})}{\sum_{i,j} P(q_{initial,i}) Z(\psi_{initial,j})}$$

where $X = q, \psi$, and χ. Note that the thermal effect plays a role in the depinning of DWs only near the critical current density.

c.   Non-uniform current distribution

When an electrical current is flowed along a metallic curved wire, the current density is not uniform along the transverse direction to the wire. This happens because (1) electrons, majority carriers in metals, would flow along the gradient of electrical potential, that is, the arc direction, and consequently (2) the resistance linearly increases with the increasing radius. For example, when a voltage V is applied to one end of curved wire having thickness t_f, mid-radius R, width w, and resistivity ρ while the other end is grounded (see fig. S4), the current dI that flows along the cross section $t_f dr$ at radius r is $dI = \frac{V t_f dr}{\pi \rho r}$. Hence the current density $J(r)$ at radius r is $J(r) = \frac{dI}{t_f dr} = \frac{V}{\pi \rho r}$, that is, $J(r) \propto \frac{1}{r}$. Hence the total current I is $I = \int_{R-\frac{w}{2}}^{R+\frac{w}{2}} dI = \int_{R-\frac{w}{2}}^{R+\frac{w}{2}} \frac{V t_f}{\pi \rho r} dr = \frac{V t_f}{\pi \rho} \log \frac{2R+w}{2R-w}$. Note that in a πR long straight wire the total current I is $I = \frac{V t_f w}{\pi \rho R}$. The fact that $\log \frac{2R+w}{2R-w} > \frac{w}{R}$ leads to that $I_{curve} > I_{straight}$ with given same length and voltage. Based on this calculation, we have implemented the non-uniform current density in Q2D model by setting $H_{SH}(r) = \frac{R}{r} H_{SH}^0$ where H_{SH}^0 is $H_{SH}(r = R)$. We will derive the Q2D equations of motion later

and discuss the parameter H_{SH}^0 in detail there. Since the conventional volume spin transfer torque (V-STT) is significantly smaller than spin-orbit torque in our system, we do not take the non-uniform current distribution effect into account in V-STT.

d. Lagrangian and Equations of Motion

First, we formulate the Lagrangians that include the adiabatic and non-adiabatic spin transfer torques, external field driven torques, the spin Hall current torque, and the Dzyaloshinskii-Moriya exchange field. The equations of motion are then derived by Lagrange-Rayleigh equations (*36*).

With the DW profile function (1), the Lagrangian $\mathcal{L}$ in the curved wire that contains the magnetostatic potential energy considering inhomogeneous anisotropy, DW kinetic energy and adiabatic spin-transfer torque is given by

$$
\begin{aligned}
\mathcal{L} = \int \int & \left[E + \frac{M_s}{\gamma} \phi \dot{\theta} \sin \theta - \frac{u M_s}{\gamma} \phi \frac{d\theta}{ds} \sin \theta \right] ds dr \\
= & \frac{2wA}{\Delta} \sec \zeta \left[1 + \left(\frac{4R^2}{4R^2 - w^2} \right) \sin^2 \zeta + \frac{\pi^2}{3} \frac{\Delta^2}{4R^2 - w^2} \right] \\
& + 2w \Delta K_{eff}^0 \left\{ 1 - \eta \cos \left[\frac{2\pi (q - q_s)}{q_0} \right] \right\} \sec \zeta + w \Delta M_s H_k \cos^2(\psi - \chi) \sec \zeta \\
& \mp 2 M_s H_z w q - \pi w \Delta M_s H_p \cos(\psi - \psi_H) \sec \zeta - \pi w \Delta M_s H_{DM} \cos(\psi - \chi) \sec \zeta \\
& \mp \frac{2w M_s}{\gamma} \phi (\dot{q} + u)
\end{aligned}
$$

$$(3)$$

Here the upper and lower signs correspond to the $\odot \mid \otimes$ and $\otimes \mid \odot$ domain magnetic configurations, respectively. s is the coordinate position along the wire length direction. $\mathcal{E}$ is the magnetostatic energy density of domain wall per area and is given by

$$\mathcal{E} = A(\nabla \vec{m})^2 + K_{eff}\left[1 - \eta \cos\frac{2\pi(q - q_s)}{q_0}\right]\sin^2\theta + \frac{M_s H_k}{2}\sin^2\theta\cos^2(\psi - \chi) - M_s H_z \cos\theta$$
$$- M_s H_p \sin\theta\cos(\psi - \psi_H) - M_s H_{DM}\sin\theta\cos(\psi - \chi)$$

$$(4)$$

Eq. (3) can be rewritten as $\mathcal{L} = \sigma + \int\int\left[\frac{M_s}{\gamma}\phi\dot{\theta}\sin\theta - \frac{uM_s}{\gamma}\phi\frac{d\theta}{ds}\sin\theta\right]dsdr$ where the

magnetostatic potential energy $\sigma = \int\int \mathcal{E}dsdr$. A is the exchange stiffness, H_k is the magnitude

of the in-plane anisotropy field derived from the shape anisotropy of the DW that favors a Bloch

DW configuration over that of a Néel wall, H_z is the out-of-plane field, H_p and ψ_H are the in-

plane magnetic field and its angle defined with respect to $+\hat{x}$ direction. H_{DM} is the

Dzyaloshinskii–Moriya interaction exchange field at the DW whose direction is always

perpendicular to DW length direction thus favoring Néel type wall but the sign depends on

domain configurations establishing the chirality of domain walls. The volume spin transfer

torque from the current within magnetic layer is parameterized by $= \frac{\mu_B PJ}{eM_s}$, where μ_B is the Bohr

magneton, e is the electron charge, P is the spin polarization of the current and J is the current

density in the magnetic layer. Note that σ is a function of DW position q, i.e. $\frac{\partial\sigma}{\partial q} \neq 0$ and a finite

pressure torque in curved wires, which is distinct from the straight wire even in the absence of

Zeeman exchange field H_z. This is due to the fact that the domain wall energy varies depending

on q since e.g. the DW tilt angle ζ changes as a function of q. Meanwhile, the dissipative

function $\mathcal{F}$ that includes damping, non-adiabatic spin-transfer torque and spin-orbit torque is

given by

$$\mathcal{F} = \int \int \frac{\alpha M_s}{2\gamma} \left[\left(\frac{d}{dt} - \frac{\beta u}{\alpha} \frac{d}{ds} \right) \vec{m} + \frac{\gamma}{\alpha} H_{SH} \vec{m} \times \hat{e}_r \right] ds dr$$

$$= \frac{\alpha M_s}{2\gamma} \left\{ \frac{2w\dot{q}^2}{\Delta} \left[\frac{w^2}{12R^2} \sin\zeta \tan^3\zeta + \cos\zeta \right] \right.$$

$$+ \frac{wq\dot{\chi}}{3R\Delta} \sin\zeta \tan\zeta \left\{ w^2 \left[\sec^2\zeta - \frac{2q}{R} \tan\zeta \right] + \pi^2\Delta^2 \sec^2\zeta \right\}$$

$$+ \frac{w\dot{\chi}^2}{6\Delta} \sec^3\zeta [w^2 + \pi^2\Delta^2 \sin^2\zeta] + 2w\Delta\dot{\phi}^2 \sec\zeta$$

$$\pm \frac{2\pi\gamma}{\alpha} H_{SH}^0 \cos\phi \left\{ \dot{q} \left[\tan^2\zeta \left(R \log\frac{2R+w}{2R-w} - w \right) + R \log\frac{2R+w}{2R-w} \right] \right.$$

$$+ \dot{\chi} R \sec^2\zeta \left(R \log\frac{2R+w}{2R-w} - w \right) \bigg\} + \frac{4\beta u}{\alpha\Delta} \dot{q} w \cos\zeta$$

$$\mp \frac{\pi\beta u}{2\alpha} \cos\phi \left\{ \dot{q} \left[\frac{1}{R} \tan^2\zeta \left(R \log\frac{2R+w}{2R-w} - w \right) + \log\frac{2R+w}{2R-w} \right] \right.$$

$$+ \dot{\chi} \sec^2\zeta \left(R \log\frac{2R+w}{2R-w} - w \right) - \frac{4\beta u\Delta}{\alpha} \dot{\phi} \sin^2\phi \sec\zeta \log\frac{2R+w}{2R-w} \bigg\}$$

$$\tag{5}$$

Here again, the upper and lower signs correspond the $\odot\,|\,\otimes$ and $\otimes\,|\,\odot$ domain magnetic configurations, respectively, β is the non-adiabatic STT coefficient. The spin Hall effect is parameterized by an effective field H_{SH}^0 in the mid-wire that is given by $H_{SH}^0 = \frac{\hbar\theta_{SH}J_{UL}}{2eM_st}$ where $\hbar$ is $\frac{h}{2\pi}$, h is Planck constant, J_{UL} is the current density in the underlayer, t is the thickness of magnetic layer, and θ_{SH} is the spin Hall angle (or the effective spin Hall angle that describes the magnitude of the spin accumulation that the magnetic layer is subjected to). Note that the accumulated spin from the spin Hall current is oriented transverse to the wire length s, i.e. the radial direction $\hat{e}_r$. The spin-orbit torque related term written in blue in Eq. (5) becomes $\pm\frac{2\pi\gamma w}{\alpha} H_{SH}^0 \dot{q} \cos\phi$ when the current distribution is uniform.

Based on Lagrangians $\mathcal{L}$ and dissipated function $\mathcal{F}$ obtained above, the Lagrange-Rayleigh equations $\frac{\partial\mathcal{L}}{\partial X} - \frac{d}{dt}\left(\frac{\partial\mathcal{L}}{\partial\dot{X}}\right) + \frac{\partial\mathcal{F}}{\partial\dot{X}} = 0$ ($X = q, \psi,$ and χ) finally lead to the equations of motion as following

$$\alpha \dot{q} \left(\frac{w^2}{12R^2} \sin \zeta \tan^3 \zeta + \cos \zeta \right) \pm \Delta \dot{\psi}$$

$$+ \frac{\alpha}{12R} \dot{\chi} \sin \zeta \tan \zeta \left[w^2 \left(\sec^2 \zeta - \frac{2q}{R} \tan \zeta \right) + \pi^2 \Delta^2 \sec^2 \zeta \right]$$

$$= \pm \gamma \Delta H_z$$

$$- \beta u \cos \zeta \pm \frac{u\Delta}{R} \pm \frac{\pi \beta u \Delta}{4w} \cos \phi \left\{ \frac{1}{R} \tan^2 \zeta \left(R \log \frac{2R + w}{2R - w} - w \right) + \log \frac{2R + w}{2R - w} \right\}$$

$$+ \frac{\beta u \Delta^2}{wR} \sin^2 \phi \sec \zeta \log \frac{2R + w}{2R - w}$$

$$- \frac{\gamma A}{RM_s} \sec \zeta \left\{ \tan \zeta \left[1 + \left(\frac{4R^2}{4R^2 - w^2} - 1 \right) \sin^2 \zeta + \frac{\pi^2}{3} \frac{\Delta^2}{4R^2 - w^2} \right] \right.$$

$$\left. + \left(\frac{4R^2}{4R^2 - w^2} - 1 \right) \sin 2\zeta \right\}$$

$$- \frac{\gamma \Delta^2}{2RM_s} \left[2K_{eff}^0 \left\{ 1 - \eta \cos \left[\frac{2\pi(q - q_s)}{q_0} \right] \right\} + M_s H_k \cos^2(\psi - \chi) \right.$$

$$\left. - \pi M_s H_p \cos(\psi - \psi_p) - \pi M_s H_{DM} \cos(\psi - \chi) \right] \sec \zeta \tan \zeta$$

$$- \frac{2\pi \gamma \eta \Delta^2}{q_0 M_s} K_{eff}^0 \sin \left[\frac{2\pi(q - q_s)}{q_0} \right] \sec \zeta$$

$$\mp \frac{\pi}{2w} \gamma \Delta H_{SH}^0 \cos \phi \left[\tan^2 \zeta \left(R \log \frac{2R + w}{2R - w} - w \right) + R \log \frac{2R + w}{2R - w} \right]$$

(6)

$$\left(\cos \zeta + \frac{\alpha \Delta}{R} \right) \dot{q} + \alpha \Delta \dot{\psi}$$

$$= -u \mp \frac{\beta u \Delta}{w} \sin^2 \phi \log \frac{2R + w}{2R - w}$$

$$\pm \frac{\gamma \Delta}{2} \left[-H_k \sin 2(\psi - \chi) + \pi H_p \sin(\psi - \psi_H) + \pi H_{DM} \sin(\psi - \chi) \right]$$

(7)

$$\frac{\alpha}{12R}\dot{q}\sin\zeta\tan\zeta\left[w^2\left(\sec^2\zeta-\frac{2q}{R}\tan\zeta\right)+\pi^2\Delta^2\sec^2\zeta\right]+\frac{\alpha}{12}\dot{\chi}\sec^3\zeta\,(w^2+\pi^2\Delta^2\sin^2\zeta)$$

$$=-\frac{\gamma A}{M_s}\sec\zeta\left\{\tan\zeta\left[1+\left(\frac{4R^2}{4R^2-w^2}-1\right)\sin^2\zeta+\frac{\pi^2}{3}\frac{\Delta^2}{4R^2-w^2}\right]\right.$$

$$\left.+\left(\frac{4R^2}{4R^2-w^2}-1\right)\sin2\zeta\right\}-\frac{\gamma\Delta^2 K_{eff}^0}{M_s}\left\{1-\eta\cos\left[\frac{2\pi(q-q_s)}{q_0}\right]\right\}\sec\zeta\tan\zeta$$

$$-\frac{\gamma\Delta^2 H_k}{2}\cos(\psi-\chi)\sec\zeta\left[\cos(\psi-\chi)\tan\zeta+2\sin(\psi-\chi)\right]$$

$$+\frac{\gamma\pi\Delta^2 H_p}{2}\cos(\psi-\psi_H)\sec\zeta\tan\zeta$$

$$+\frac{\gamma\pi\Delta^2 H_{DM}}{2}\sec\zeta\left[\sin(\psi-\chi)+\cos(\psi-\chi)\tan\zeta\right]$$

$$\mp\frac{\gamma\Delta\pi R H_{SH}^0}{2w}\cos\phi\sec^2\zeta\left(R\log\frac{2R+w}{2R-w}-w\right)$$

$$+\frac{\Delta\pi\beta u}{8w}\sec\zeta\left(R\log\frac{2R+w}{2R-w}-w\right)$$

$$\tag{8}$$

Here again, the upper and lower signs correspond the $\odot\,|\,\otimes$ and $\otimes\,|\,\odot$ domain magnetic configurations, respectively. For cases of uniform current distribution, the spin-orbit torque related terms written in blue in Eqs. (6) and (8) become $\mp\frac{\pi}{2}\gamma\Delta H_{SH}^0\cos\phi$ and 0, respectively.

When $R\to\infty$, the Eqs. (6)-(8) become

$$\frac{\alpha\cos\chi_s}{\Delta}\dot{q}\pm\dot{\psi}=\pm\gamma H_z-\frac{2\pi\gamma\eta\Delta^2}{q_0 M_s}K_{eff}\sin\frac{2\pi(q-q_s)}{q_0}\sec\chi-\frac{\beta u}{\Delta}\cos\chi\mp\frac{\pi}{2}\gamma H_{SH}\cos\psi$$

$$\tag{9}$$

$$\frac{\cos\chi_s}{\Delta}\dot{q}\mp\alpha\dot{\psi}=-\frac{u}{\Delta}\cos\chi\mp\frac{\gamma}{2}H_k\sin2(\psi-\chi)\pm\frac{\pi}{2}\gamma H_p\sin(\psi-\psi_H)\pm\frac{\pi}{2}\gamma H_{DM}\sin(\psi-\chi)$$

$$\tag{10}$$

$$\frac{\pi^2}{6\gamma}\alpha M_s\Delta\left[\left(\frac{w}{\Delta\pi}\right)^2\sec^2\chi+\tan^2\chi\right]\dot{\chi}$$

$$=-\left[\frac{2A}{\Delta}+2K_{eff}\Delta+M_sH_k\Delta\sin(\psi-\chi)+\pi M_sH_{DM}\Delta\cos(\psi-\chi)\right]\tan\chi$$

$$-H_kM_s\Delta\sin2(\psi-\chi)+\pi\Delta M_sH_p\sin(\psi-\psi_H)+\pi\Delta M_sH_{DM}\sin(\psi-\chi)$$

$$(11)$$

These Eqs. (9)-(11) correspond to the equations of motion for straight wires (*28*).

Note that for straight wire, the magnetostatic potential energy σ does not depend on q so that the pressure torque driven DW velocity $v_{pressure}=-\frac{\alpha\gamma\Delta}{2M_s}\frac{\partial\sigma}{\partial q}$ is zero in the absence of H_z and periodic variation of anisotropy. However, in curved wires, σ is a function of q entirely due to curvature effect, i.e., $v_{pressure}\neq0$, even when $H_z=0$ and $\eta=0$.

e.   Current driven domain wall dynamics in curved wires

Now based on the newly developed Q2D model above, let us investigate the current driven DW motion in curved wires. First, we will discuss the DW dynamics in the absence of non-uniform current distribution (NUCD). Before starting the discussion one may wonder how the velocity along the DW profile would evolve as a function of time during the application of current pulses since the DW length would increase indefinitely if the velocity is same all along the DW. This can be understood by extending an analogy to the dynamics of a disk with mass M and radius R, whose center of mass (CM) is at the CM velocity v_{CM} while the disk rotates with angular velocity ω around the CM in the static Cartesian coordinates. (see fig. S6A). Note that the kinetic energy is divided to drive (1) the linear motion of CM and (2) the rotation of disk, which gives rise to top instantaneous velocity $v_{top}=v_{CM}+R\omega$ that is larger than the bottom instantaneous velocity $v_{bottom}=v_{CM}-R\omega$. In the same way, the energy to drive the DW motion by current in a curved wire is used not only to move the mid-radius of DW at velocity $\dot{q}$ but to rotate the DW around the mid-point of DW at angular velocity $-\dot{\chi}$. Hence the velocity at the outer and inner rims in DW would be $\dot{q}-\frac{w}{2}\dot{\chi}$ and $\dot{q}+\frac{w}{2}\dot{\chi}$, respectively, and in general $\dot{q}-(r-R)\dot{\chi}$ at a radius r (see fig. S6B). This shows that the velocity $\dot{q}$ is

compensated by $-(r - R)\dot{\chi}$ at r. In particular, when $\dot{\chi} = -\frac{\dot{q}}{R}$, the velocity becomes fully

compensated, which corresponds to the steady state of tilt angle $\zeta = \frac{q}{R} + \chi$, i.e., $\dot{\zeta} = 0$. In the

steady state, the velocity $v(r) = \dot{q} - (r - R)\dot{\chi} = \dot{q} + (r - R)\frac{\dot{q}}{R} = \frac{r}{R}\dot{q}$ at r in DW (see fig.

S6C) and the angular velocity $\frac{v(r)}{r} = \frac{\dot{q}}{R}$ at r, that is, independent of r. This implies that the

angular velocity is uniform along the DW in the steady state (see fig. S6B,D). Note that the

Q2D model calculation in fig. S6D shows that the angular velocity does not look completely

constant along the DW. This is because the DW does not fully reach the steady state within the

pulse length $t_p = 50$ ns.

Our Q2D model calculation shows that curvature dependence of current driven DW motion is

due to the fact that $\left|\frac{3\pi}{2} - \phi_{ud}\right| \sim \left|\frac{3\pi}{2} - \phi_{du}\right|$ while ζ_{ud} is significantly larger than ζ_{du}. This

happens because (1) ϕ relaxes in much shorter time scale than ζ (28) and (2) the magnetostatic

potential energy favors negative χ in $\odot \mid \otimes$ configuration whilst a positive χ value is favored

in $\otimes \mid \odot$. These mechanisms induce $\left|\frac{3\pi}{2} - \phi_{ud} + \zeta_{ud}\right| > \left|\frac{3\pi}{2} - \phi_{du} + \zeta_{du}\right|$, $\zeta_{ud} - \chi_{ud} - \frac{3\pi}{2} <$

0, and $\zeta_{du} - \chi_{du} - \frac{3\pi}{2} > 0$ so that the H_{DM} driven torque $\left|\tau_{DM}^{ud}\right| < \left|\tau_{DM}^{du}\right|$ and the H_k driven

torque $\left|\tau_{H_k}^{ud}\right| > \left|\tau_{H_k}^{du}\right|$ where τ_{H_k} has opposite sign to τ_{DM}, since $\tau_{DM} \propto \cos\left(\frac{3\pi}{2} - \phi_{ud} + \zeta_{ud}\right)$

and $\tau_{H_k} \propto \sin 2\left(\frac{3\pi}{2} - \phi_{ud} + \zeta_{ud}\right)$. As a result, $\tau_{DM}^{ud} + \tau_{H_k}^{ud} < \tau_{DM}^{du} + \tau_{H_k}^{du}$. As either the width

increases or the radius decreases, $|\zeta_{ud} - \zeta_{du}|$ increases thus increasing the differences in DW

velocity between two domain configurations (see fig. S5 and S7).

In the presence of the NUCD, the DW dynamics are further affected because the outer radius

the wire is subject to the smaller current density as discussed above thus increasing tilt angle ζ

compared to the absence of NUCD. Actually our Q2D model has an additional term that is

responsible for NUCD in the eq. of motion related to the tilt angle dynamics, which is written

in blue in Eq. (8). This term is always positive thus increasing the tilt angle since $H_{SH} > 0$,

$\cos\phi < 0$ ($\odot \mid \otimes$), and $\cos\phi > 0$ ($\otimes \mid \odot$) that leads to

$$\mp \frac{\gamma \Delta \pi R H_{SH}^0}{2w} \cos \phi \sec^2 \zeta \left(R \log \frac{2R+w}{2R-w} - w \right) > 0$$ irrespective of domain configurations and sign

of H_{SH}. The increased ζ is clearly observed in fig. S12 (also see fig. S8 as a reference). It is remarkable that the NUCD induced torque depends on the domain configurations. It is found that NUCD in DW motion plays a key role in depinning DWs trapped in pinning potential that is more dominant for $\otimes \mid \odot$ than $\odot \mid \otimes$ because the NUCD tends to increase ζ more for $\otimes \mid \odot$ thus enlarging the difference of DW velocity between two configurations near the threshold current density J_c (see fig. S9). In particular, the increased tilt angle ζ for $\otimes \mid \odot$ configuration changes the sign of τ_{H_k} that comes to have the same sign as τ_{DM} because $\zeta_{du} - \chi_{du} - \frac{3\pi}{2} < 0$ thus τ_{H_k} being added to τ_{DM}. As a result, v_{DU} is still larger than v_{UD}.

Note that the pressure torque driven DW velocity $v_{pressure}$ is small although it is not simply zero because $\frac{\Delta}{R} \ll 1$ (see fig. S10B and S11B).

f.   Comparison with micromagnetic simulations

Micromagnetic simulations of current driven DW motion in curved nanowires have been carried out using LLG micromagnetics simulator (*29*). Due to the memory intensiveness of simulating a wire of the same size as our experiment, we simulated a wire which was smaller in dimension (w=0.4 μm, R=1 μm). We have then initialized two magnetic configurations for running our simulation with the domain wall in the middle of the wire. After sending an electrical pulse with the current density 1.0 x 10^8 A/cm^2, we see that that a $\otimes \mid \odot$ DW responds differently than a $\odot \mid \otimes$ consistent with our understanding and experimental observations. The micromagnetic simulation results are in excellent agreement with Q2D model calculations that use the same parameters (see. fig. S13).

g.   Curvature dependence of DW motion in narrow nanowires

It is relevant to know if the curvature still influences the DW motion of narrow nanowires when the widths of nanowires are rather small (~ a few tens of nanometers) in practical devices with high density. Hence to answer this question we calculate the DW velocity for various radii of

curvature R= 100, 125 and 175 nm at fixed width w=50 nm, which correspond to the same ratio

of $\frac{R}{w}$ for R=4, 5 and 7 µm at fixed w=2 µm that are shown in Fig. 2A&B and Fig. 3C&D. It is

clear that the DW velocity is different depending on the curvature although the difference is

smaller than the wider wires (see fig. S16). However, this difference in narrow wires is critical

thus preventing the proper operation of racetrack device as the lockstep motion independent of

DW configuration is essential.

2.   Definition of Curvature in curved wires

In differential geometry, the curvature κ in a curved line $\vec{r}(s) = (x(s), y(s))$ that is a function of

a parameter s in the $x - y$ plane can be defined as

$$\kappa = \frac{\frac{dy}{ds}\frac{d^2x}{ds^2} - \frac{dx}{ds}\frac{d^2y}{ds^2}}{\left[\left(\frac{dx}{ds}\right)^2 + \left(\frac{dy}{ds}\right)^2\right]^{3/2}}$$

(10)

Since the DW position q is constrained to lie within the nanowire, we choose q to describe the

curved nanowire $\vec{r}(s)$. The time t can be used for s, so we set $s = t$. Since $\vec{r}(t) =$

$\left(R \sin\frac{q}{R}, R \cos\frac{q}{R}\right)$ (see fig. S1A) and $q = vt$ in the steady state, then $\vec{r}(t) = \left(R \sin\frac{vt}{R}, R \cos\frac{vt}{R}\right)$.

Finally using $\frac{d\vec{r}(t)}{dt} = \left(v \cos\frac{vt}{R}, -v \sin\frac{vt}{R}\right)$, and $\frac{d^2\vec{r}(t)}{dt^2} = \left(-\frac{v^2}{R} \sin\frac{vt}{R}, -\frac{v^2}{R} \cos\frac{vt}{R}\right)$ then we find

from Eq. (10), that the curvature κ is given by

$$\kappa = \frac{1}{R}\frac{v}{|v|}$$

(11)

Eq. (11) shows that the curvature κ is positive (negative) when the DW moves clockwise (counter-clockwise). Similarly, if we choose the current density J to be a parameter that describes $\vec{r}(t)$, then we find
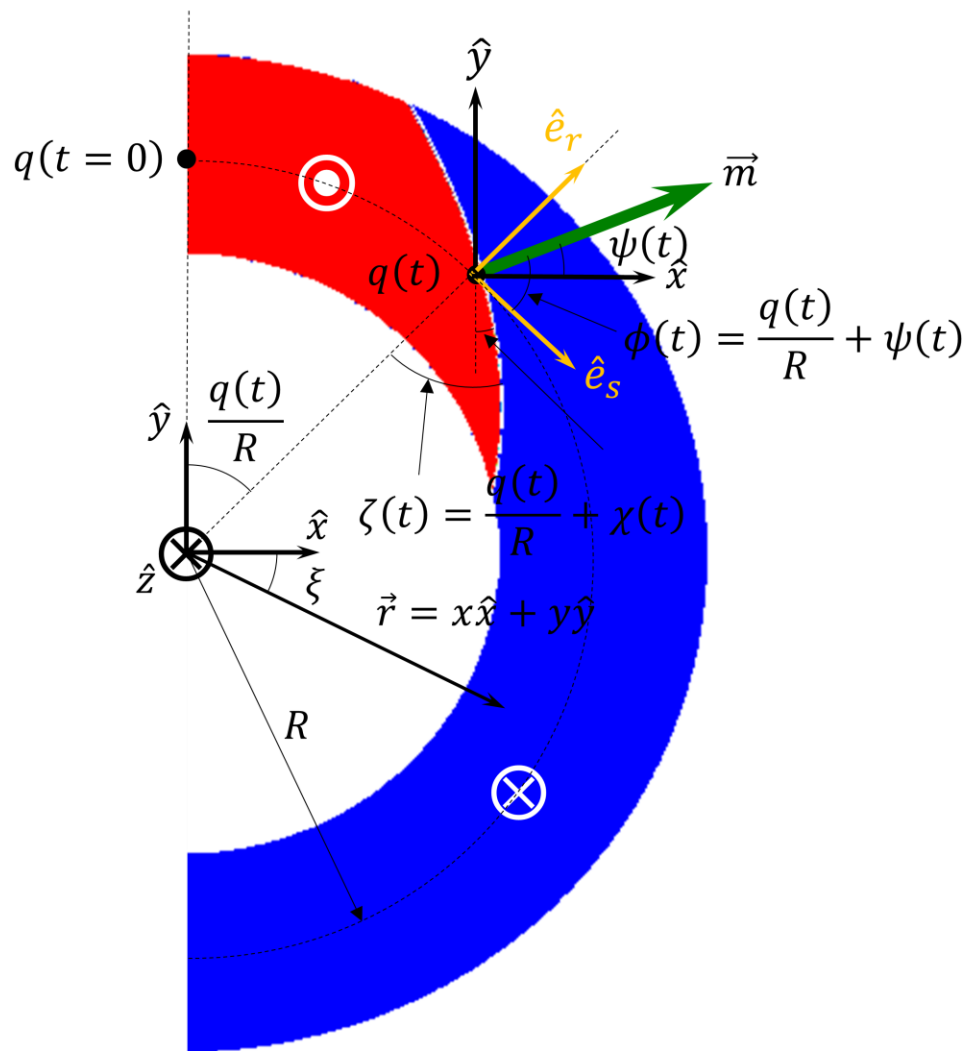
$$\kappa = \frac{1}{R}\frac{J}{|J|}$$

(12)

Likewise the curvature κ is positive (negative) when the current flows clockwise (counter-clockwise). The tables in fig. S15A and B are made using these two definitions of curvature, respectively.

Supplementary Figure captions

A

$q(t=0)$

$\hat{e}_r$

$\vec{m}$

$\psi(t)$

$\hat{x}$

$q(t)$

$\hat{y}$

$\phi(t) = \dfrac{q(t)}{R} + \psi(t)$

$\hat{e}_s$

$\hat{y} \quad \dfrac{q(t)}{R}$

$\hat{x}$

$\zeta(t) = \dfrac{q(t)}{R} + \chi(t)$

$\hat{z}$

ξ

$\vec{r} = x\hat{x} + y\hat{y}$

R

B

θ

$\vec{m}$
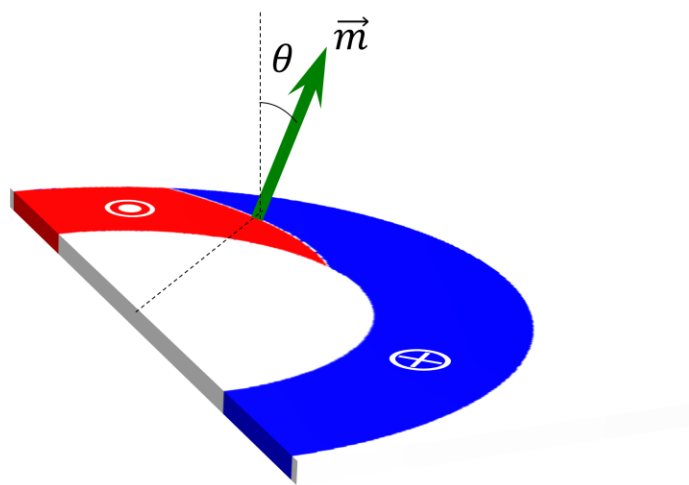
Figure S1

fig. S1. Schematic illustration of basic parameters used in the Q2D model for current driven domain wall motion. Schematic illustration of basic parameters used in the Q2D model for current driven domain wall motion in top view of curved wires with $\odot \,|\, \otimes$ domain configuration: (**A**) top view and (**B**) slanted overview. The moving frame coordindates $\hat{e}_s$, $\hat{e}_r$ and $\hat{z}$ are cartooned together with the static Cartesian coordinates $\hat{x}$, $\hat{y}$ and $\hat{z}$.
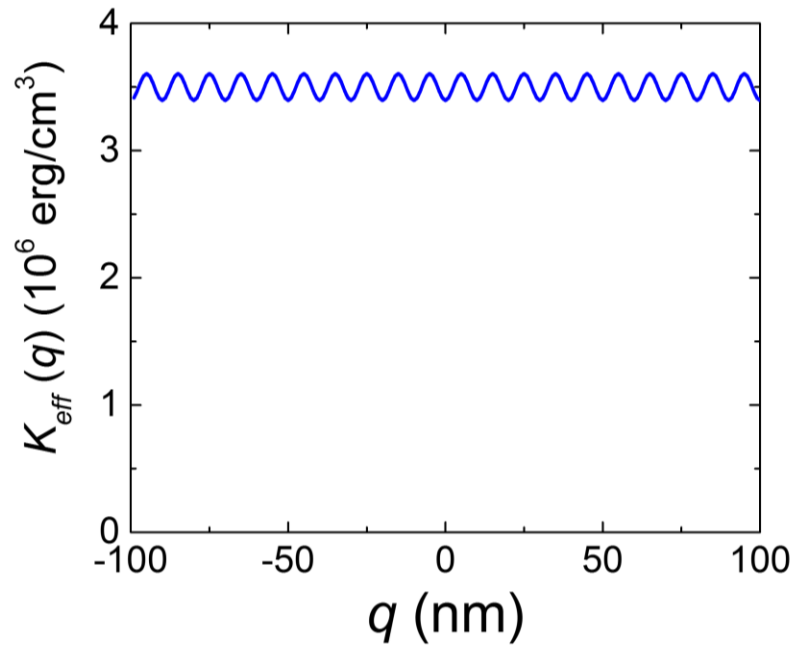
Figure S2

fig. S2. Profile of anisotropy constant $K_{eff}(q)$ with $K_{eff}^0 = 3.5 \times 10^6$ erg/cm³, $\eta = 0.03$, $q_s = 0$ nm, and $q_0 = 10$ nm.
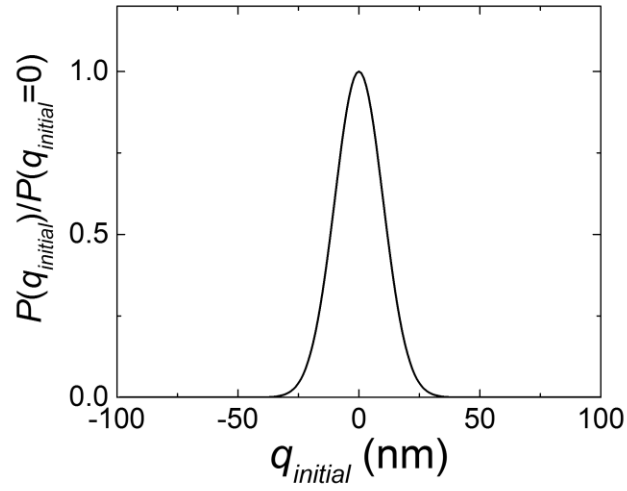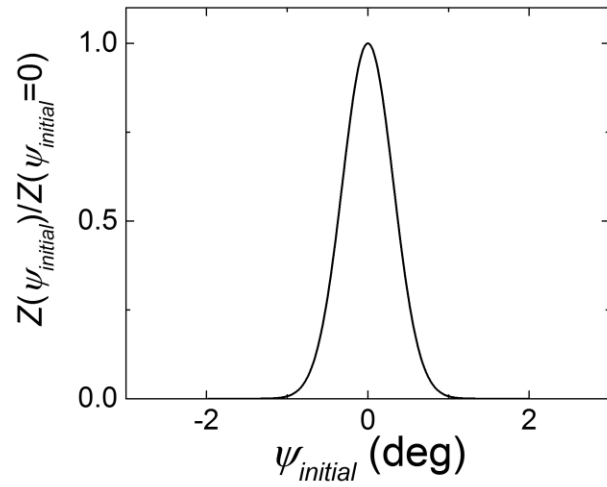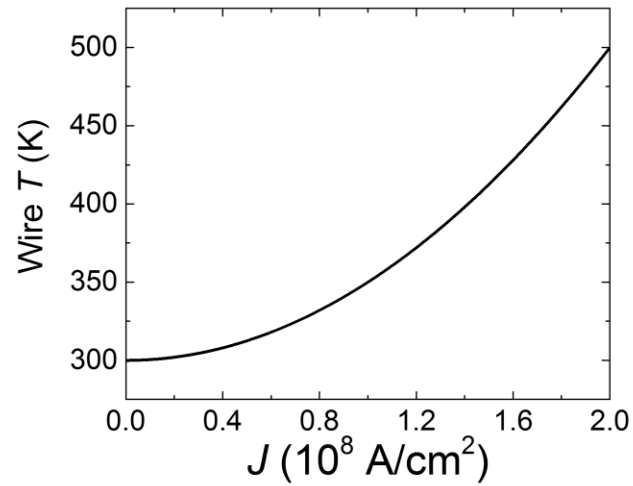
Figure S3

fig. S3. Modeling of thermal broadening. Profile of normalized (**A**) $P(q_{initial})$ and (**B**) $Z(\psi_{initial})$ with T=500K, H_{c0}=20 Oe, q_0=10 nm, Δ=5 nm, M_s=580 Oe, w=2 µm, and t=1 nm. (**C**) Plot of wire temperature vs. current density J.
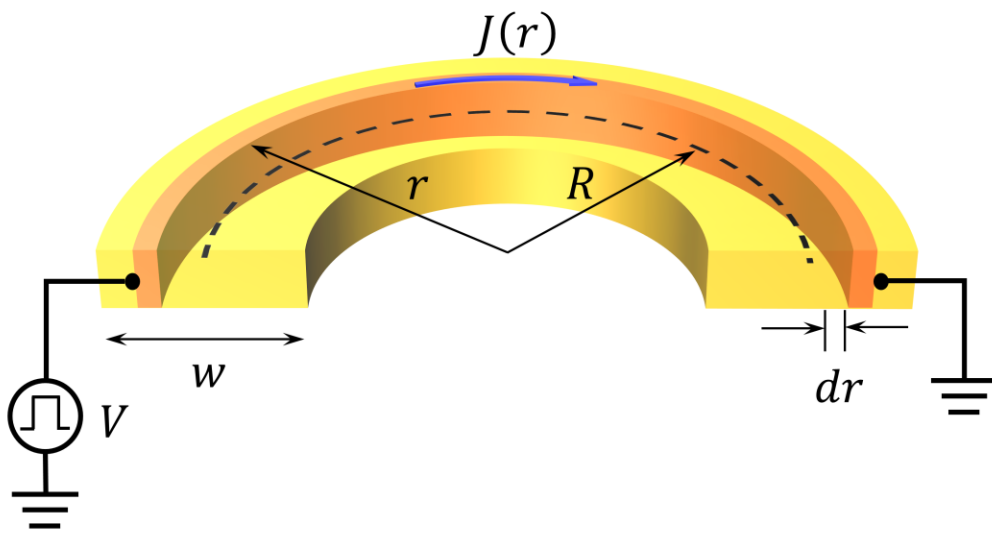
Figure S4

fig. S4. Schematic of current distribution in curved wire with width w and mid-radius R. A voltage V is applied on the left end while the right end is grounded.
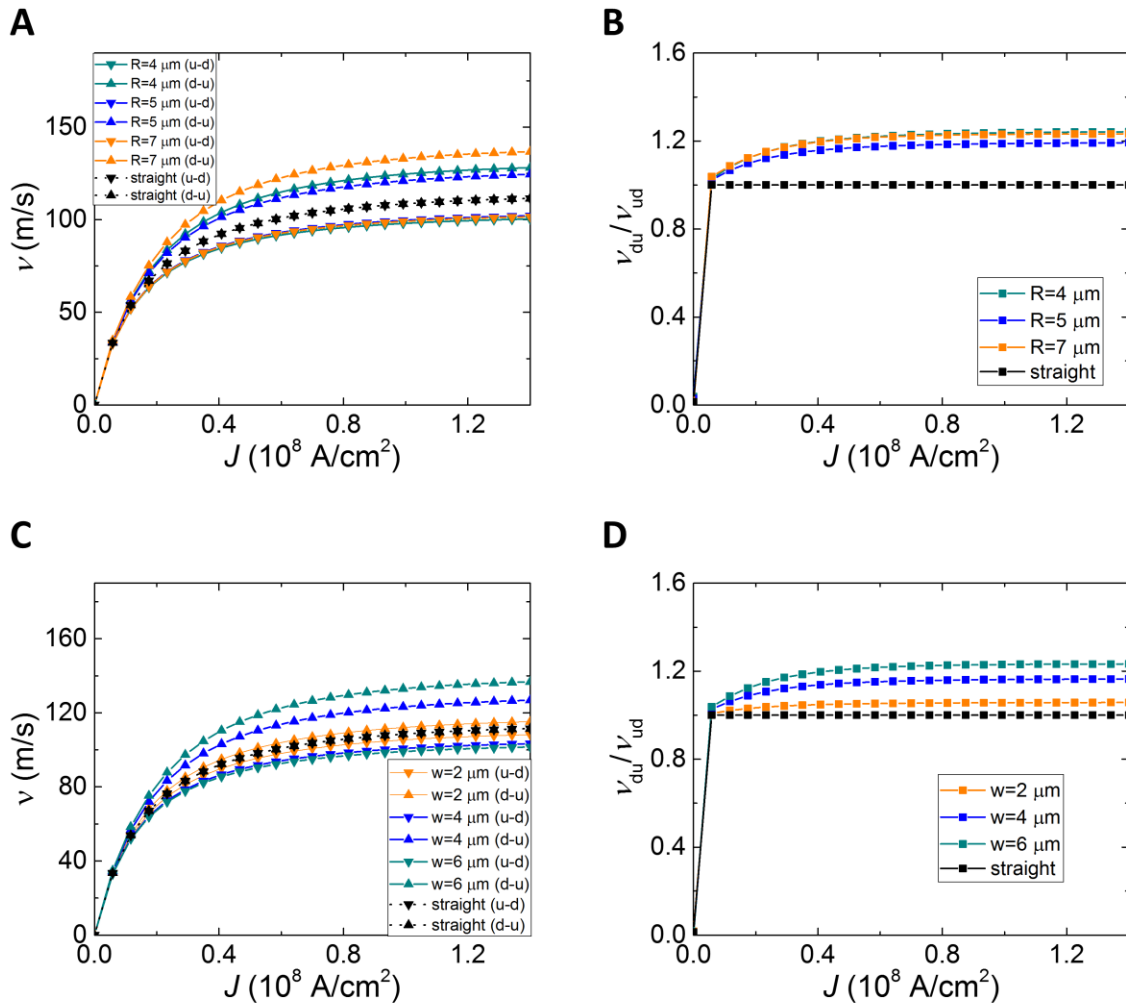
Figure S5

fig. S5. Plots of Q2D model calculation results that take neither nonuniform current distribution nor pinning and thermal fluctuation into account. (**A,C**) DW velocity v, (**B,D**) DW velocity ratio $\frac{v_{du}}{v_{ud}}$, vs. J. (**A,B**) R=4, 5, and 7 μm while w is fixed at 2 μm. (**C,D**) w=2, 4, 6 μm while R is fixed at 16 μm. The commonly used parameters for all calculation are Δ=5 nm, t_p=50 ns, α=0.1, β=0, η=0, K_{eff}=3.5×10^6 erg/cm^3, H_k=1,000 Oe, $H_{SH}(J = 1.4 \times 10^8 A/cm^2)$=700 Oe, H_{DM}=1,000 Oe, M_s=580 emu/cm^3.

A

$$v_{top} = v_{CM} + R\omega$$

v_{CM}

R

M

ω

$$v_{bottom} = v_{CM} - R\omega$$

B

$$\dot{q} - \frac{w}{2}\dot{\chi}$$

$$v = \dot{q} - (r - R)\dot{\chi}$$

$\dot{q}$

$$\dot{q} + \frac{w}{2}\dot{\chi}$$

$\dot{\zeta} = 0$

$-\dot{\chi}$

ζ

r

ζ

R

w

C

v (m/s)

r (μm)

- ▼ U-D
- △ D-U

D

$v(r) / r$ (rad/s)

r (μm)

- ▼ U-D
- △ D-U
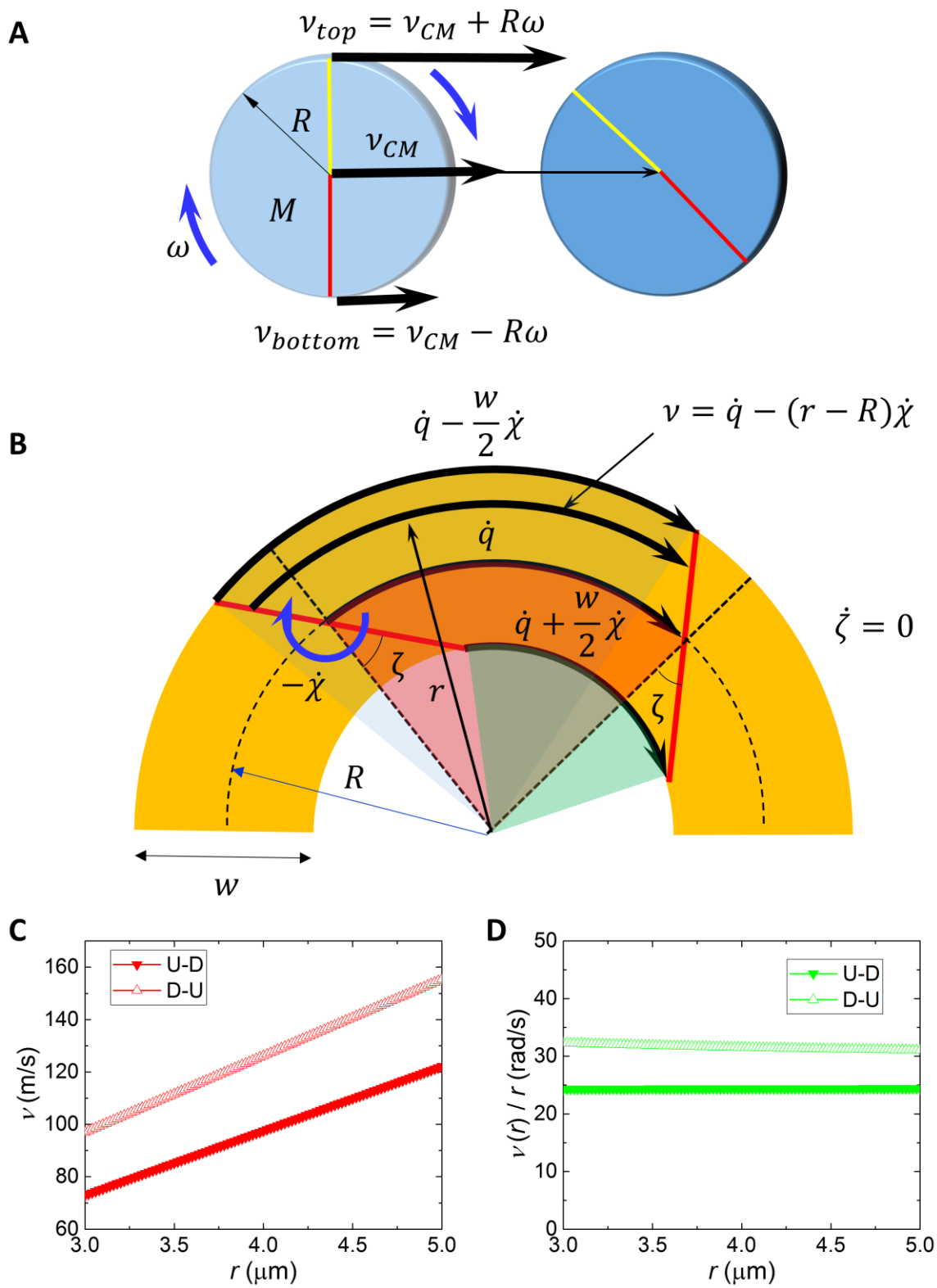
Figure S6

fig. S6. Radial dependence of DW velocities transverse to the curve wire direction. (**A**) Schematic of a rigid solid disk whose CM at the CM velocity v_{CM} while the disk rotates with angular velocity ω around the CM in the static Cartesian coordinates. (**B**) Schematic of tilted DW development against time in the curved wire that is in the steady state, i.e., $\dot{\zeta} = 0$. While the midpoint of DW moves at velocity $\dot{q}$, the DW itself rotates around the midpoint at angular velocity $-\dot{\chi}$ in the static Cartesian coordinates. The shaded pie shapes correspond to the solid angles covered by displacement of 4 points in DW during a certain time. (**C**) Plot of DW velocity at each point along the transverse to the wire versus radius. (**D**) Plot of DW angular velocity at each point along the transverse to the wire versus radius. The parameters used in calculation for plots of (**C,D**) are same as used in fig. S5 except w=2 μm and R=4 μm.
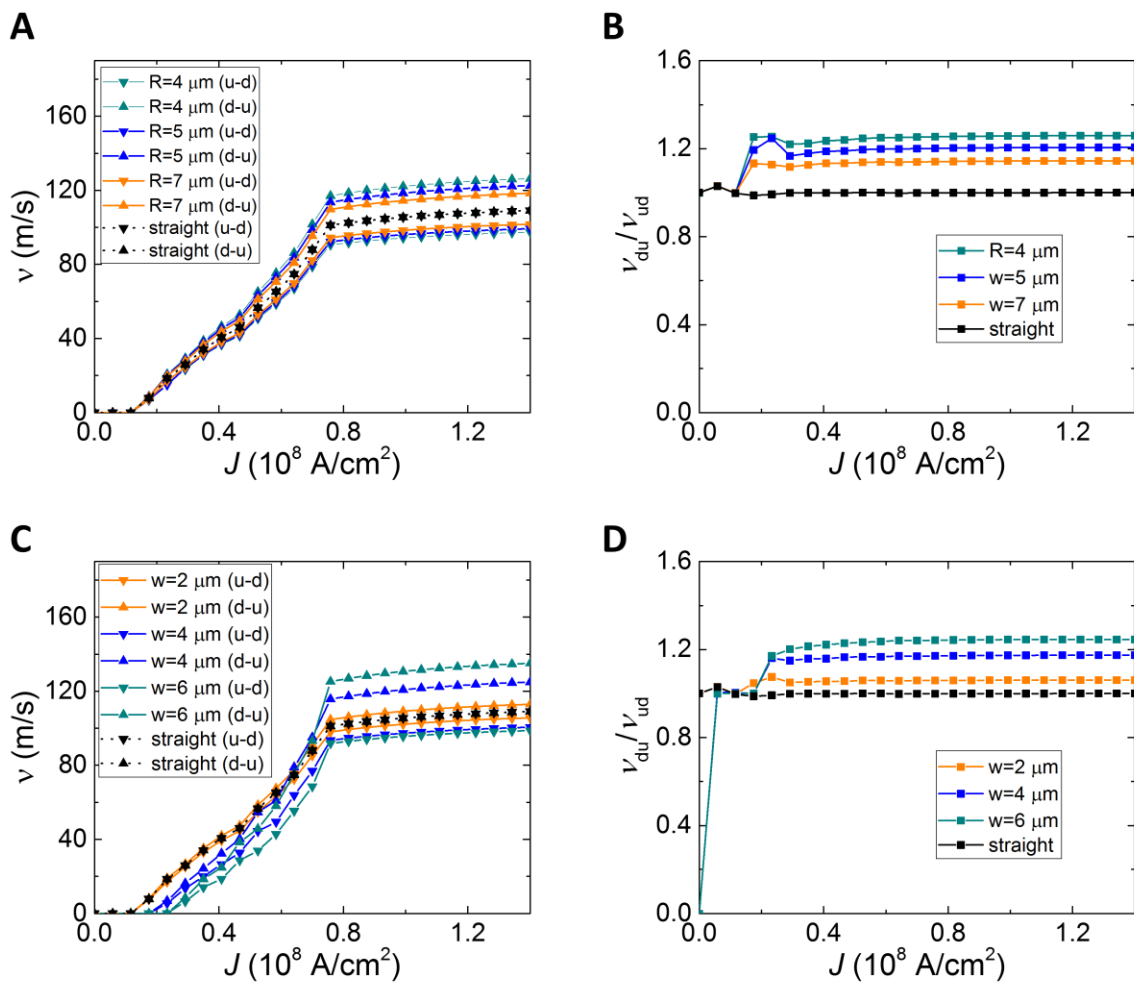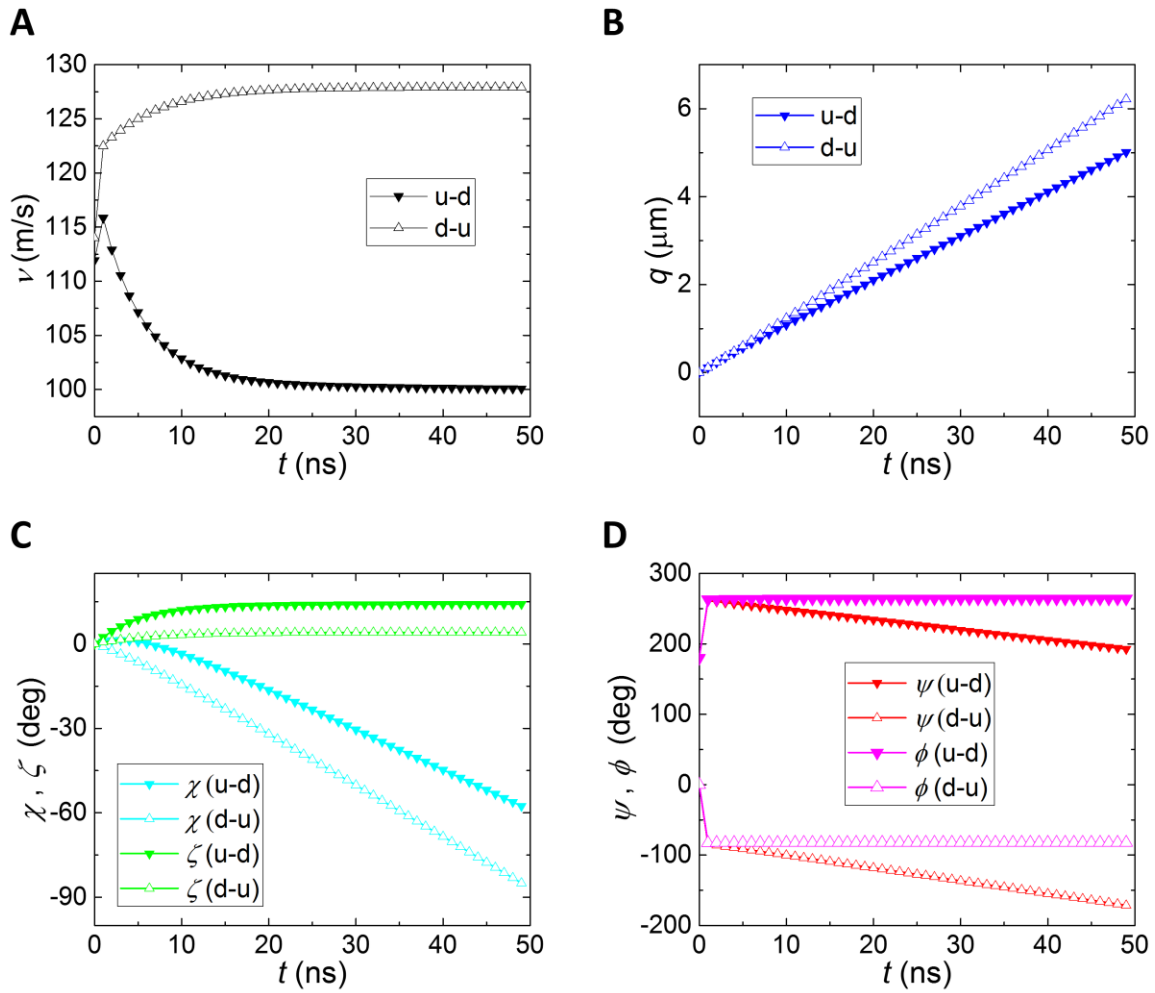
Figure S7

fig. S7. Plots of Q2D model calculation results that take pinning and thermal fluctuation but no nonuniform current distribution into account. (**A**,**C**) DW velocity v, (**B**,**D**) DW velocity ratio $\frac{v_{du}}{v_{ud}}$, vs. J. All the parameters are same as used in fig. S5 except H_{c0}=20 Oe, η=0.03, q_s=0 nm, and q_0=10 nm. The variation curve of temperature T against J shown in fig. S3 is used to incorporate the thermal fluctuation effect.

Figure S8

fig. S8. Plots of time-resolved Q2D model calculation results that take pinning and thermal fluctuation but no nonuniform current distribution into account. (**A**) DW velocity v, (**B**) DW position displacement q, (**C**) DW tilt angles χ and ζ, (**D**) DW magnetization angles ψ and ϕ vs. t. All the parameters are same as used in fig. S7 except w and R are fixed at 2 and 4 µm, respectively.
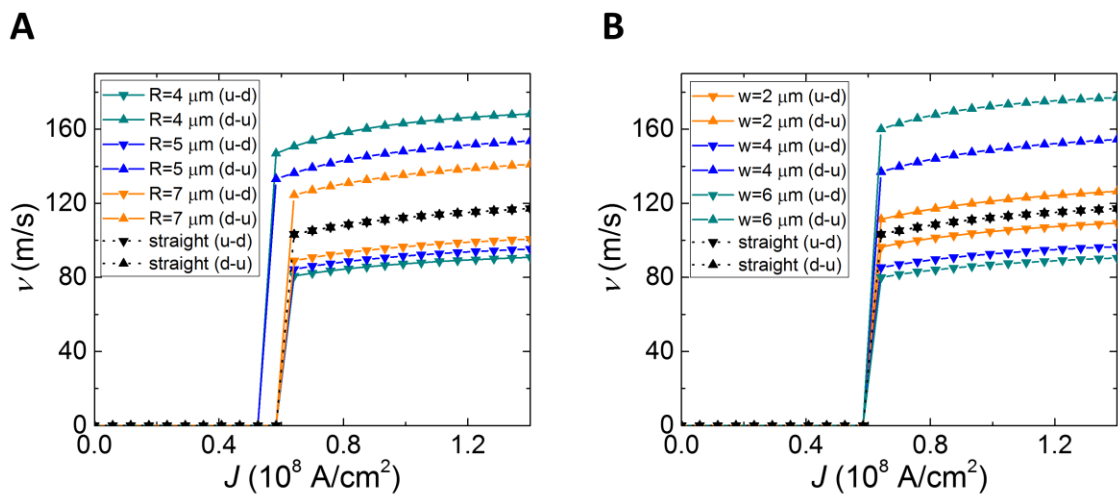
A

B

Figure S9

fig. S9. Plots of Q2D model calculation results that take nonuniform current distribution and pinning, but no thermal fluctuation into account. (**A,B**) DW velocity v. All the parameters are same as used in fig. S5 except H_{c0}=20 Oe, η=0.03, q_s=0 nm, and q_0=10 nm.
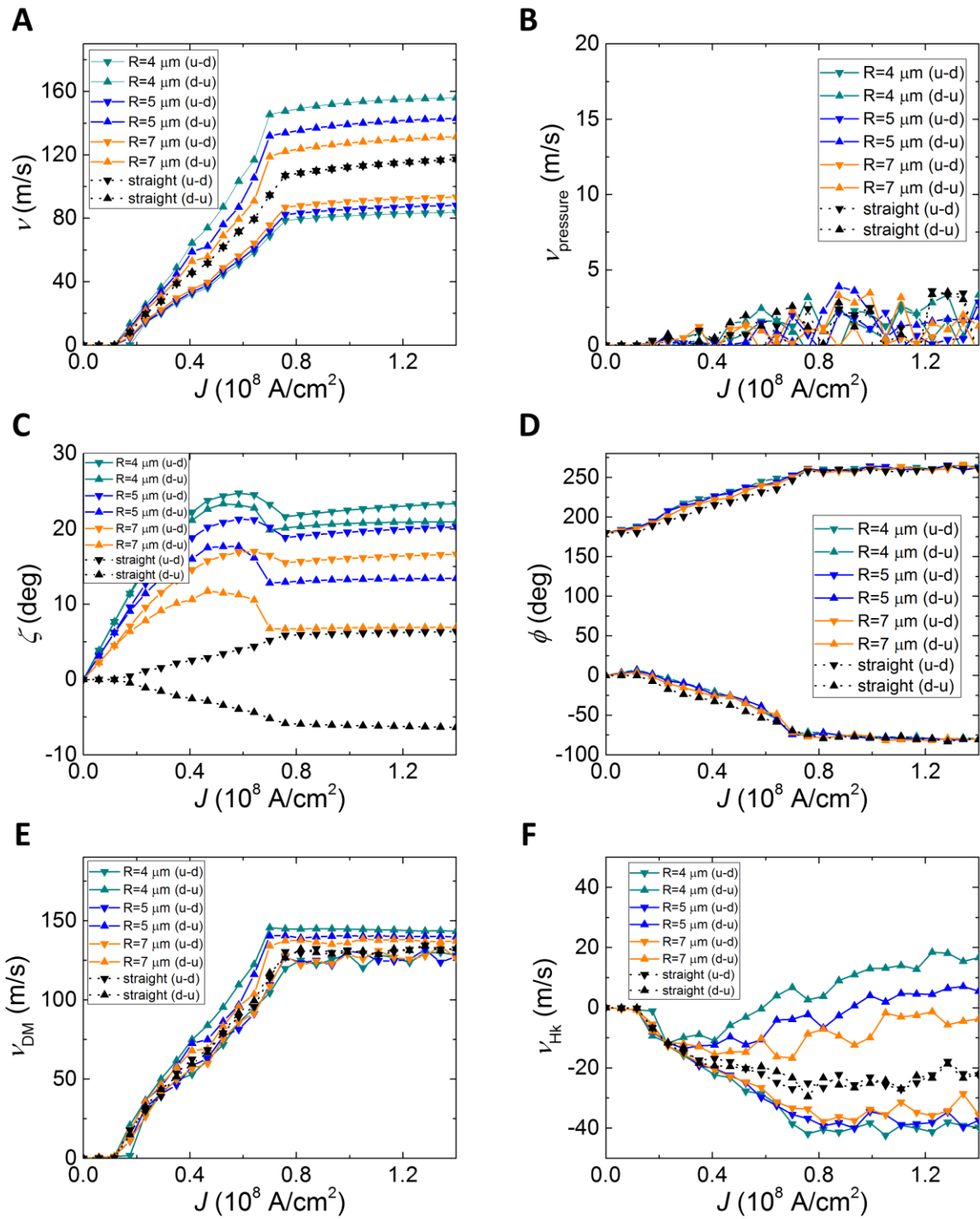
Figure S10

fig. S10. Plots of Q2D model calculation results that take nonuniform current distribution, pinning, and thermal fluctuation into account for various radii while width is fixed. Plots of Q2D model calculation results that take *non-uniform current distribution, pinning and thermal fluctuation* into account for $R=4$, 5, and 7 µm while w is fixed at 2 µm: (**A**) DW velocity v, (**B**) DW velocity driven by pressure torque only, $v_{pressure}$, (**C**) DW tilt angle ζ, (**D**) DW magnetization angle ϕ, (**E**) DW velocity driven by H_{DM} only, v_{DM} and (**F**) DW velocity driven by H_k, v_{H_k} vs. J. All the parameters are same as used in fig. S5 except $H_{c0}=20$ Oe, $\eta=0.03$, $q_s=0$ nm, and $q_0=10$ nm. The variation curve of temperature T against J shown in fig. S3 is used to incorporate the thermal fluctuation effect.
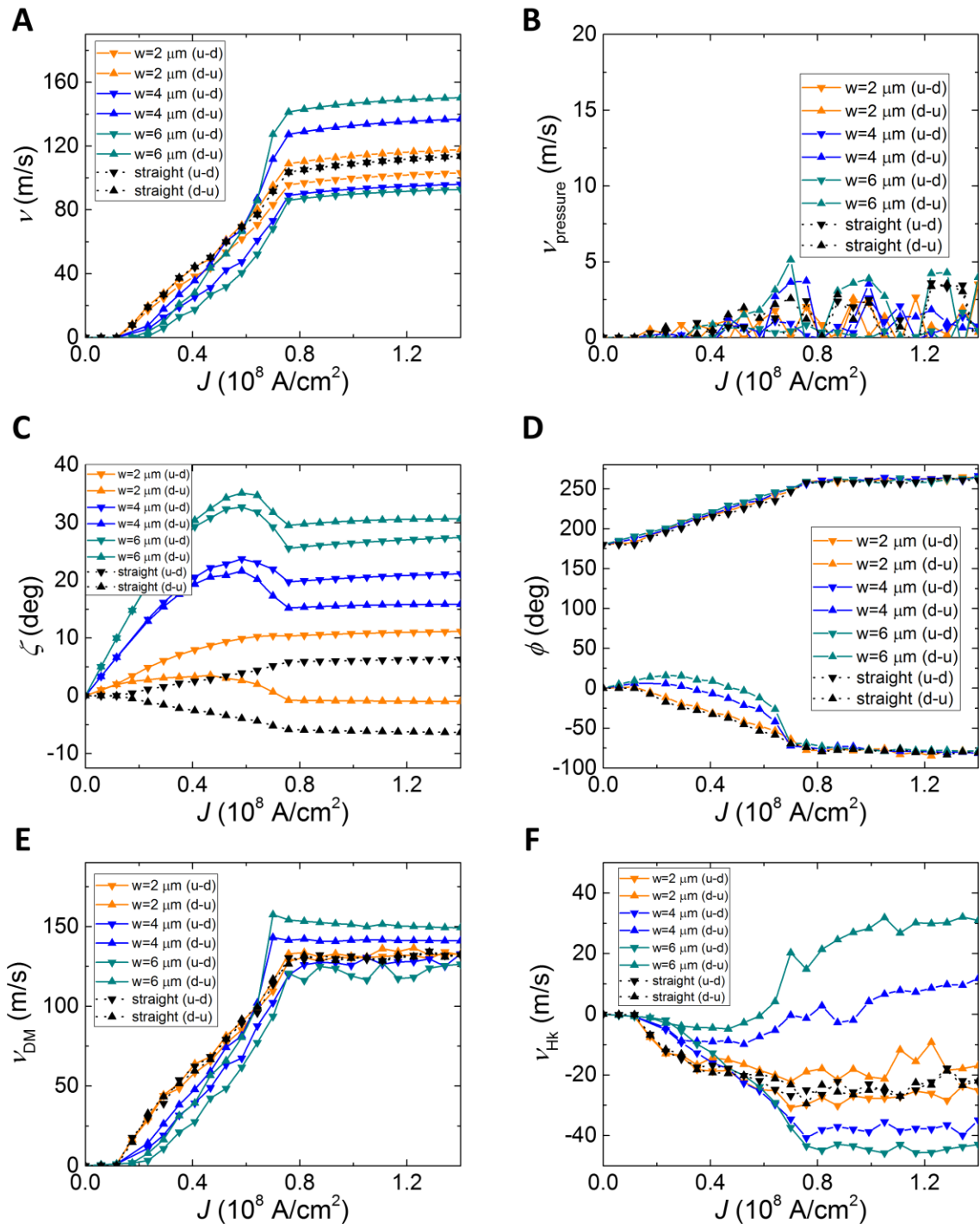
Figure S11

fig. S11. Plots of Q2D model calculation results that take nonuniform current distribution, pinning, and thermal fluctuation into account for various widths while the radius is fixed. Plots of Q2D model calculation results that take *non-uniform current distribution, pinning and thermal fluctuation* into account for $w=2, 4, 6$ μm while R is fixed at 16 μm: (**A**) DW velocity v, (**B**) DW velocity driven by pressure torque only, $v_{pressure}$, (**C**) DW tilt angle ζ, (**D**) DW magnetization angle ϕ, (**E**) DW velocity driven by H_{DM} only, v_{DM} and (**F**) DW velocity driven by H_k, v_{H_k} vs. J. All the parameters are same as used in fig. S5 except $H_{c0}=20$ Oe, $\eta=0.03$, $q_s=0$ nm, and $q_0=10$ nm. The variation curve of temperature T against J shown in fig. S3 is used to incorporate the thermal fluctuation effect.
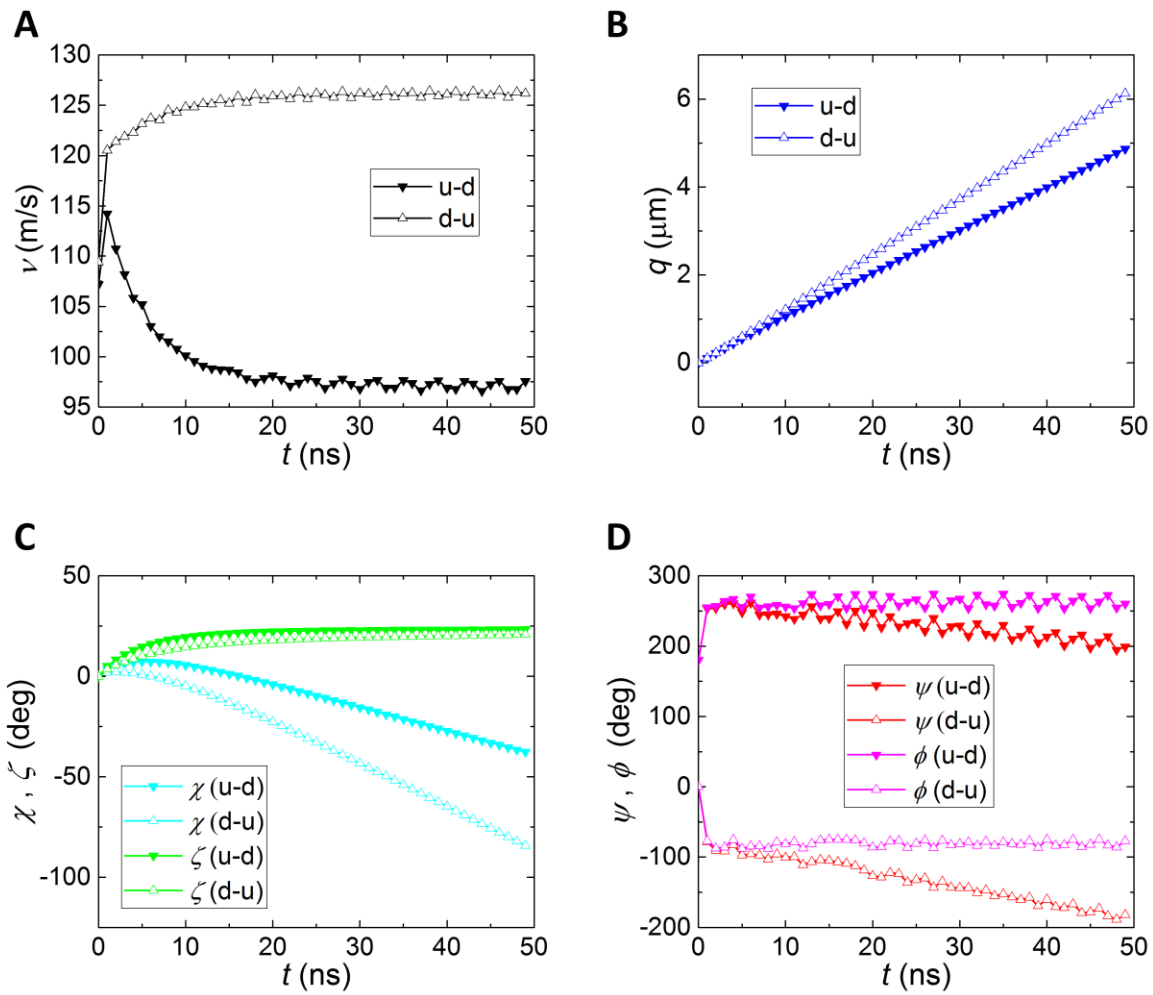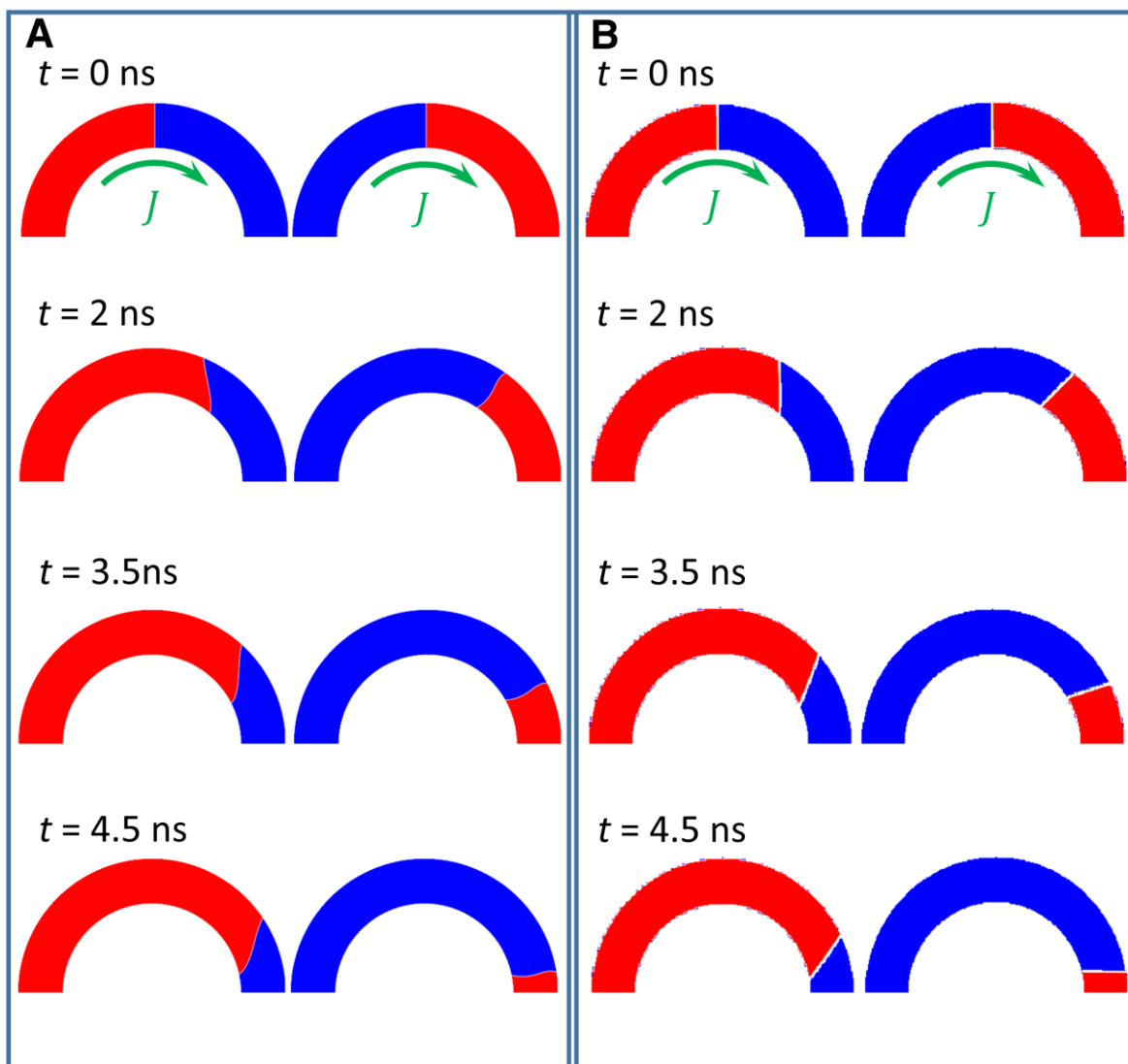
Figure S12

fig. S12. Plots of time-resolved Q2D model calculation results that take pinning and thermal fluctuation but no nonuniform current distribution into account. (**A**) DW velocity v, (**B**) DW position displacement q, (**C**) DW tilt angles χ and ζ, (**D**) DW magnetization angles ψ and ϕ vs. t. All the parameters are same as used in fig. S10 except w and R are fixed at 2 and 4 µm, respectively.

Micromagnetic   Q2D model

A

$t = 0$ ns

J J

$t = 2$ ns

$t = 3.5$ns

$t = 4.5$ ns

B

$t = 0$ ns

J J

$t = 2$ ns

$t = 3.5$ ns

$t = 4.5$ ns

m_z -1 +1

Figure S13

fig. S13. Comparison of micromagnetic simulations and Q2D model. Snapshots of (**A**) micromagnetic simulations and (**B**) Q2D model calculations at time t=0, 2, 3.5 and 4.5 ns since the onset of current pulse application. For both the simulations, the NUCD and the following parameters are employed: ferromagnetic layer thickness t_f is 1.5 nm, the DMI parameter $D = -1$ erg/cm^2, M_S = 580 emu/cm^3, K_{eff} =5.11×10^6 erg/cm^3, A =0.75 μerg/cm, $\alpha = 0.1$, w=0.4 μm, R=1 μm, the current density J=1.0×10^8 A/cm^2, and spin Hall angle θ_{SH}=0.1. As for the micromagnetic simulations the used cell size is 2.5 nm x 2.5 nm x 1.5 nm, and the spin Hall layer that is placed under the ferromagnetic layer is chosen to be 1.5 nm thick.
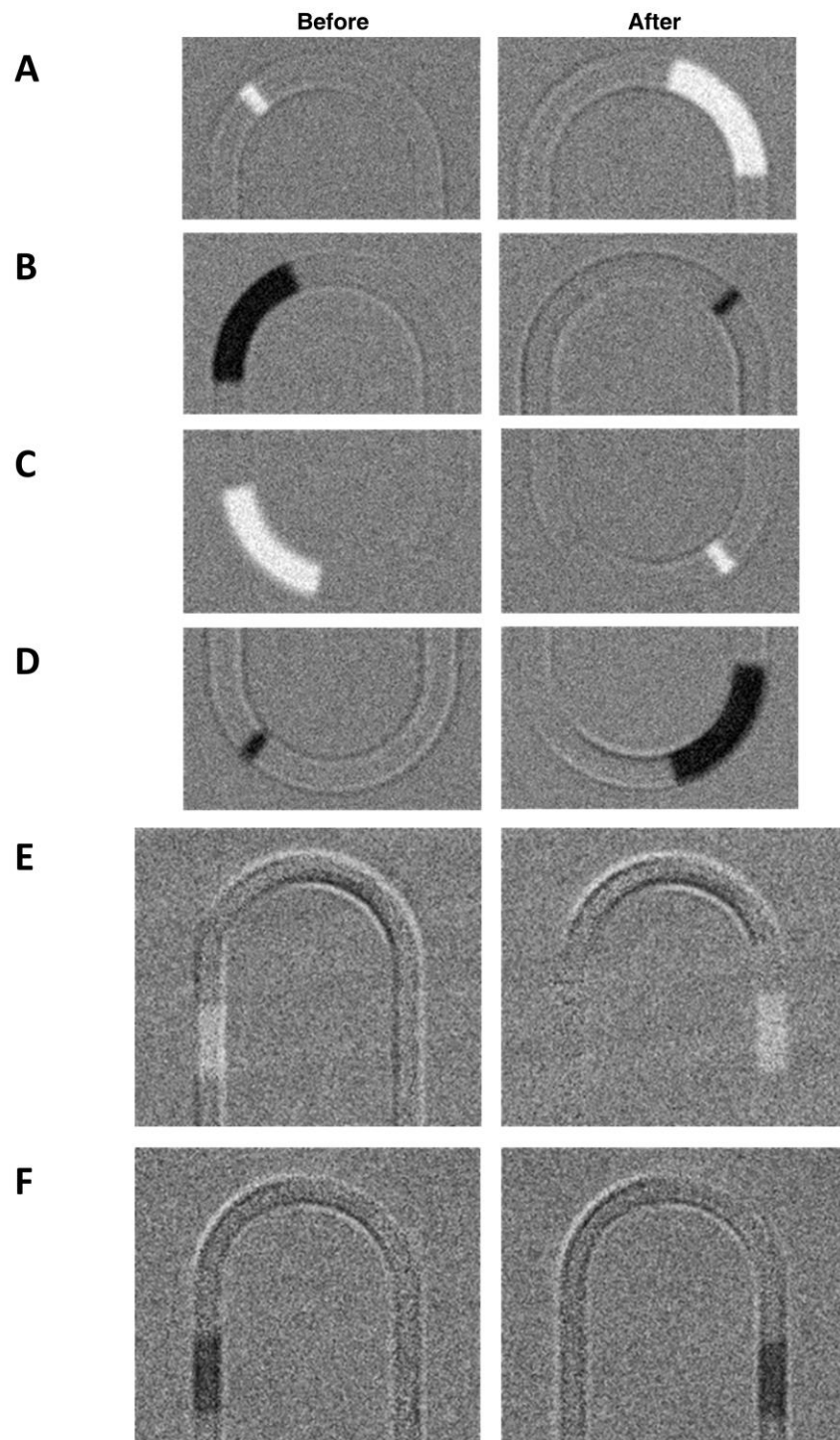
Before   **After**

A

B

C

D

E

F

Figure S14

fig. S14. Unabridged Kerr images corresponding to the main text. The left side shows the Kerr image of a magnetic domain in the magnetic nanowire before the application of electrical pulses and the right portion shows the Kerr images after the application of electrical pulses. (**A-D**) correspond to Fig. 1B. (**E,F**) correspond to Fig. 4A**.**

Figure S15

fig. S15. Schematic table outlines the relationship between the effect of curvature on the DW velocity (⊙|⊗ or ⊗|⊙), which is found to be independent of the sign of DMI or SHE. Depending on the evolution of DW tilt w.r.t track curvature, a DW can either go faster or slower due to the change in effective DMI torque. A DW goes faster if it tilts in the direction of the bend and goes slower if it tilts opposite to that. Changing the sign of either the DMI or SHE torque not only changes the direction of DMI-induced tilting but also the sign of curvature which is why the same relationship still holds. (**A**) when the curvature is defined w.r.t. motion, (**B**) when the curvature is defined w.r.t. current.
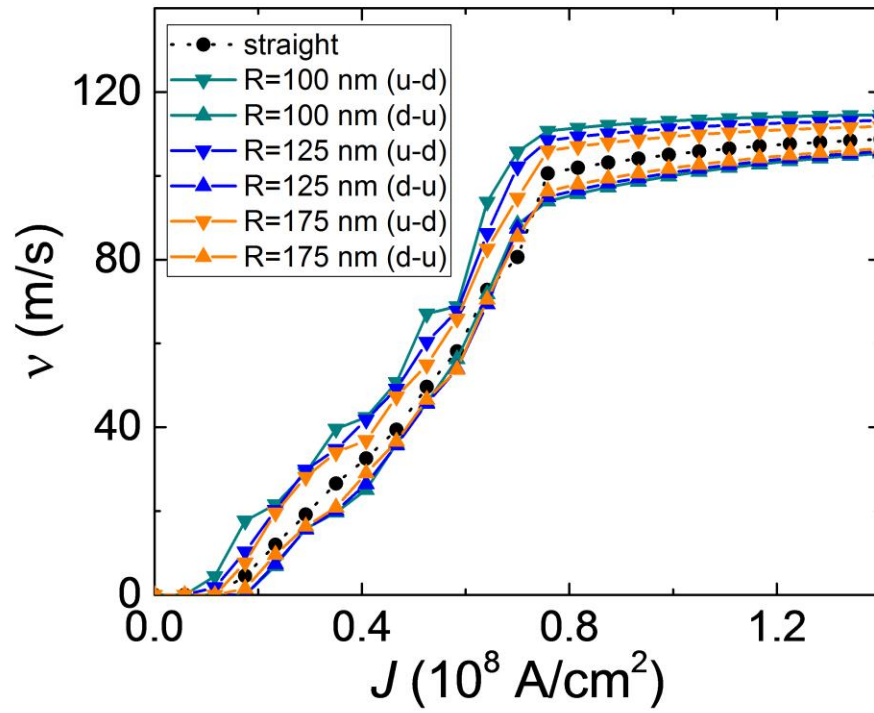
Figure S16

fig. S16. *v* **against** *J* **of the quasi-2D model calculation results that take nonuniform current distribution, pinning, and thermal fluctuation into account for** *R* **= 100, 150, and 175 nm while** *w* **is fixed at 50 nm.** All the parameters are same as used in fig. S5 except H_{c0}=20 Oe, η=0.03, q_s=0 nm, and q_0=10 nm.

movie S1. Animation of Q2D calculation of time resolved DW motion in curved nanowires with positive curvatures for various radii and widths. Q2D calculation of time resolved DW motion in curved nanowires with positive curvatures and (**A**) R=4, w=2, (**B**) R=5, w=2, (**C**) R=7, w=2, (**D**) R=16, w=2, (**E**) R=16, w=4, and (**F**) R=16, w=6 μm. The parameters used in the calculations are same as fig. S10 and S11.